Hybridized Metal Slit Eigenmodes as an Illustration of Babinet's Principle

Burcu Ögüt,[†,*] Ralf Vogelgesang,[‡] Wilfried Sigle,[†] Nahid Talebi,[†,§] Christoph T. Koch,[†] and Peter A. van Aken[†]

[†]Max Planck Institute for Intelligent Systems, Heisenbergstrasse 3, 70569 Stuttgart, Germany, [‡]Max Planck Institute for Solid State Research, Heisenbergstrasse 1, 70569 Stuttgart, Germany, and [§]Photonics Research Laboratory, Center of Excellence for Applied Electromagnetic Systems, School of Electrical and Computer Engineering, University of Tehran, North Kargar Avenue, Tehran, Iran

ABSTRACT By energy-filtering transmission electron microscopy (EFTEM), we observe Fabry-Pérot-like surface plasmon resonances (SPRs) along the length of rectangular single and double slits drilled into free-standing thin silver films. These eigenmodes hybridize in closely situated slits. The nature of their lateral coupling is uncovered from finite-element simulations, which show that the symmetry and energy sequence of hybrid modes is governed by Babinet complementarity principles. Interestingly, the modes of a double slit system, being proto-self-complementary, may alternatively be explained by magnetic interactions between slit fields or by electrostatic interactions across the metallic bridge separating the slits.

KEYWORDS: surface plasmon resonances · energy-filtering transmission electron microscopy · finite-element method · Babinet's principle · silver rectangular slits

The rising demand of nanoscale electronic and photonic applications[1,2] has been an impetus for plasmonics to become an emerging field of nanotechnology over the past decade, especially attracting attention in the fields of cancer diagnostics[3] and therapy,[4] surface-enhanced Raman spectroscopy,[5] optical circuitry,[6] and plasmonic computer systems.[7] Since the pioneering studies of Pines and Bohm[8] and Ritchie,[9] it has been known that some part of the energy losses of electrons passing through thin films is due to plasmon excitations, which are coherent collective oscillations of the electron liquid in a conductor intertwined with associated electromagnetic fields. Surface plasmons (SPs) are waves propagating along a metal/dielectric interface, whereas surface plasmon resonances (SPRs) are the corresponding eigenmodes in confined systems.[10] The SPR energy and optical properties, such as scattering and absorption, can be tuned by modifying the geometry.

Surface plasmons[11] can be excited if fast electrons pass a dielectric medium in a transmission electron microscope (TEM)—as first demonstrated in 1982 by Batson.[12] Most importantly, the investigation by fast electrons offers very high spatial resolution in the range of a few nanometers, which is presently not easily achieved with light optical techniques.[13] Not until recently has it become possible to image localized surface plasmon resonances (LSPRs) in the entire wavelength range from far-infrared up to the ultraviolet.[14] In particular, the far-infrared regime has become more readily accessible by the introduction of narrow band-pass electron monochromators. In the work presented here, we make use of an imaging energy filter that allows us to directly acquire images at selected energy losses corresponding to LSPRs. So far, this method has been applied on nanotriangles,[15−17] nanorods,[18] and arrangements of circular nanoholes[19,20] to directly map their plasmonic eigenmodes. Here we apply it to rectangular nanoslits. The advantages of this geometry are (i) that the object is free-standing so that substrate effects do not have to be considered in the analysis and (ii) that the very fine spatial sampling allows wavenumbers of SP modes to be measured directly from the as-acquired raw experimental images.

The main emphasis of this article is how electromagnetic coupling affects the LSPR energies in a slit system. It is well-known that surface plasmon coupling effects can be mediated by both the electric and magnetic field components.[21] Figure 1a(i) shows the charge distribution of a LSPR of a single thin metallic rod with negative real part, ε_1, of the dielectric function. Owing to the negative sign of ε_1 (which is typical for metals in the optical wavelength range), the low-energy mode has the same charges on both sides of the rod. The situation is quite similar in the case of surface plasmons on a thin film.[22] If the film thickness is of similar magnitude as the skin depth, the electric field components on both surfaces interact, leading to the well-known (low-energy) symmetric and (high-energy) antisymmetric surface modes. Magnetic field

* Address correspondence to ogut@is.mpg.de.

Received for review June 17, 2011 and accepted July 15, 2011.

Published online July 15, 2011
10.1021/nn2022414

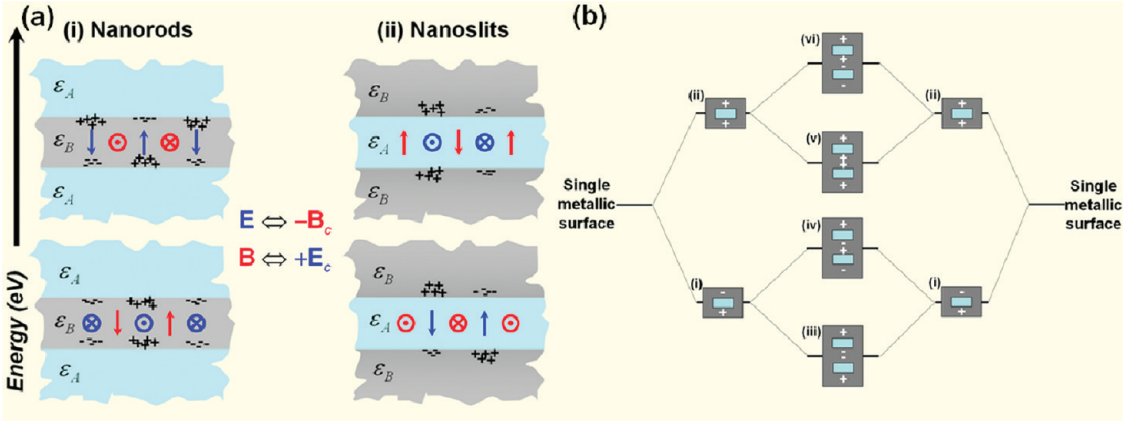

Figure 1. (a) Babinet principle, relating the fields diffracted (or scattered) by (i) nanorods and by (ii) complementary nanoslits. Schematically illustrated here are selected field components in a plane on the "shadow" side close by but not coinciding with the object plane. Blue and red colors indicate electric and magnetic fields, respectively. (b) Expected plasmon hybridization scheme for metallic slits.

components are relatively weak in the case of rods, which explains why the interaction of closely spaced rods can be described in a quasi-static electric picture.[23,24]

If we now look at the complementary system, namely, a slit in a metal film (Figure 1a(ii)), opposite charges on both sides have minimum energy because the medium between the charges is air (or vacuum) with $\varepsilon_1 > 0$. It is obvious that in Figure 1a(ii) there is now a strong magnetic moment in the slit center pointing into and out of the image plane. Therefore, the role of magnetic fields in coupled slits can be expected to be strong. This may also be regarded as a direct consequence of Babinet's principle[25−27] which states that the role of electrical and magnetic fields is interchanged in complementary systems.[21]

The electromagnetic coupling possibilities of two metallic surfaces can be analyzed with a scheme in Figure 1b based on plasmon hybridization theory.[28] As two independent silver surfaces approach each other forming a rectangular slit, the primarily observed electromagnetic surface modes will blend and the antisymmetric (mode i) and symmetric (mode ii) charge distributions will be observed at lower and higher energies, respectively, in agreement with Figure 1a(ii). Two single slits that have antisymmetric charge distributions hybridize in two different manners. The low-energy and high-energy modes are expected to have the charge distributions of $+ - - +$ and $+ - + -$, respectively (modes iii and iv). Hybridization of two single slits with symmetric charge distribution is supposed to form two modes with charge distribution of $+ + + +$ at lower energy and $+ + - -$ at higher energy, respectively (modes v and vi). In principle, symmetric and antisymmetric single slit modes (modes i and ii in Figure 1b) might hybridize, but as their energies are usually far away from each other, hybridization of these two modes with different symmetry configurations is not energetically feasible in practice.[29] We will come back to these considerations about Babinet's principle and plasmon hybridization while discussing the experimental results.

RESULTS AND DISCUSSION

We first discuss results for single slits. In Figures 2 and 3, selected images from the EFTEM series and the corresponding results obtained from the high-frequency structure simulator (HFSS 12) simulations are displayed. Energy-loss probability in the EFTEM images and electrical field magnitude in the simulation results are color-coded in such a way that they increase from blue to yellow color (see color bars). From the electric field divergence extracted from Figures 2c and 3b, we deduce the distribution of charges for the different eigenmodes around the single and double slit configuration; "+" and "−" signs are used in Figures 2 and 3 to mark the central position of the charges.

Pronounced intensity maxima are visible along the long (y) direction in both the experimental EFTEM images and the simulated electric field magnitudes. We start the discussion for the case of the single slit. The experimental data (Figure 2a,b) exhibit maxima at the top and bottom edges of the slit. Their separation is, within the experimental error, equidistant for a given energy loss (or wavelength). The intensity profiles in Figure 2b prove that the number of maxima are two at 1 eV (1.24 μm), three at 1.4 eV (0.89 μm), and four at 1.8 eV (0.69 μm), substantiated with the line profile of the electric field distributions in Figure 2d, as well. (Note that the mode exhibiting only one maximum could not be detected because of its low eigenenergy, which was screened by the tail of the zero-loss peak.) In the following, we denote these modes as α, β, and δ. The electric field distributions obtained from the simulations show the same shape as the experimental data. Figure 2c shows that at 1 eV (1.24 μm), 1.19 eV (1.04 μm), and 1.62 eV (0.76 μm) the electric field vectors oscillate in phase (symmetric) along the x direction, corresponding

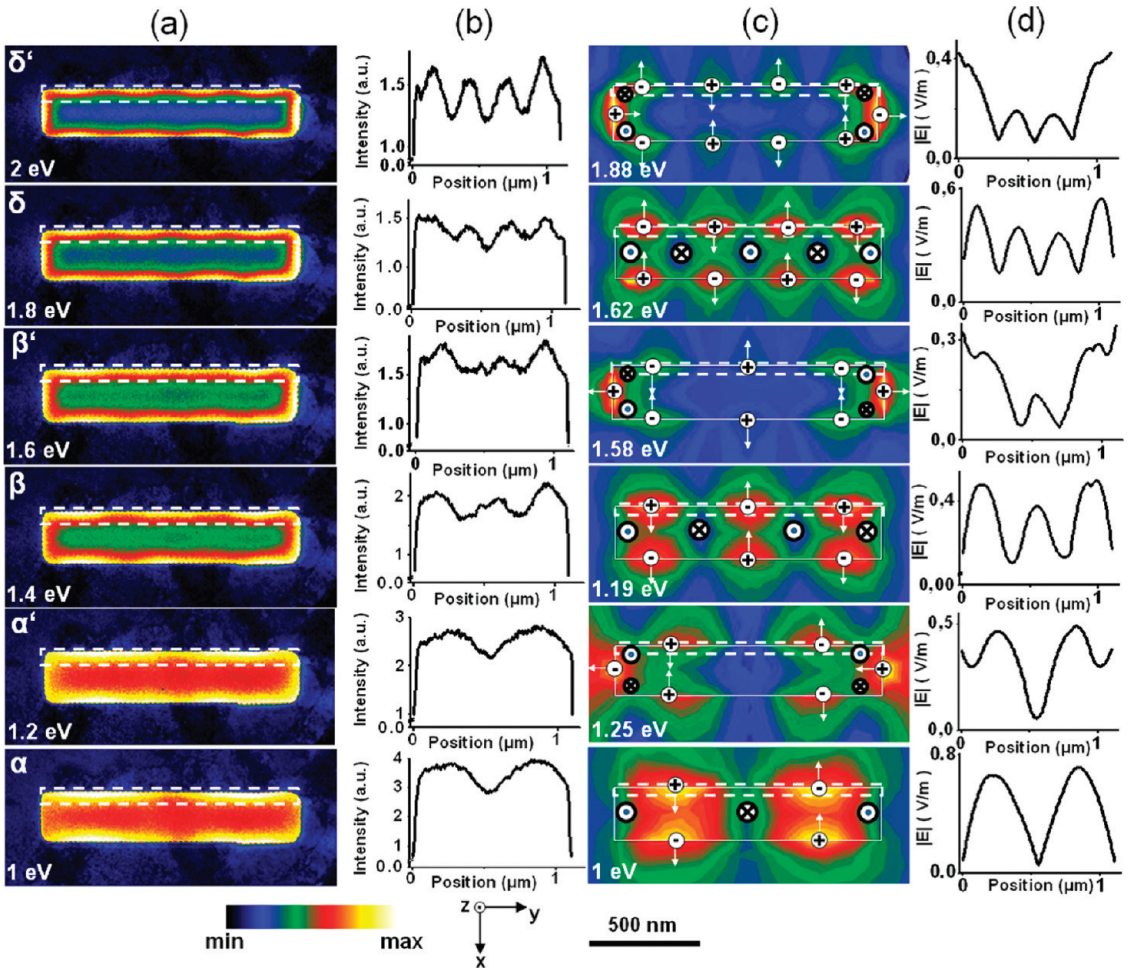

Figure 2. (a) Experimental EFTEM images acquired at the energy-loss range of 1−2 eV; (b) intensity profiles along the regions marked in the EFTEM images; (c) calculated electric field strength |E| vectors (black arrows), charge distributions and magnetic field vectors (pointing into and out of the page assigned by ⊗ and ⊙, respectively) at resonance energies (wavelengths) of 1 eV (1.24 μm), 1.25 eV (0.99 μm), 1.19 eV (1.04 μm), 1.58 eV (0.78 μm), 1.62 eV (0.76 μm), and 1.88 eV (0.66 μm); and (d) calculated electric field profiles along the regions marked in the simulated images for the single slit. The scale bar is also valid for both (a) and (c).

to the accumulation of opposite electrical charges on both sides of the long slit walls, thereby giving rise to a dipolar, capacitor-like behavior.[30] The modes, designated as α', β', and δ' at 1.25 eV (0.99 μm), 1.58 eV (0.78 μm), and 1.88 eV (0.66 μm), respectively, reveal that the same charge distribution is observed along the long slit walls as for the mode α, β, and δ, but that the electric field vectors are oscillating out of phase. These modes are not so visible in the experimental results, due to the fact that these modes are weak. In addition, the experimental energy resolution is limited to 0.2 eV.

We now consider the case of two closely spaced slits (Figure 3a,b). From the experimental data (Figure 3a), we see that the field distribution is not the same along the outer and inner long slit walls, contrary to the case for the single slits—a first indication of strong interaction of the electromagnetic fields of the two slits leading to mode hybridization. Calculated field distributions (Figure 3b) confirm that the equal charges associated with the symmetric electrical field vectors add coherently and cause an electrical field enhancement at the connecting bridge at 0.95 eV (1.29 μm) (mode α*), 1.15 eV (1.08 μm) (mode β*), and 1.58 eV (0.79 μm) (mode δ*). In contrast, at 1.04 eV (1.19 μm) (mode α**), 1.27 eV (0.98 μm) (mode β**), and 1.82 eV (0.68 μm) (mode δ**), the electric field at the bridge is rather weak, in accordance with a cancellation of opposite charges. The electromagnetic field is therefore concentrated along the outer edges of the slits.

Apart from the intriguing contributions of eigenmodes leading to Fabry-Pérot-like standing wave patterns along the length of the nanoslits, notable symmetries emerge in the field patterns across, associated with Babinet complementarity. Whereas a single slit is the unmistakable Babinet complement of a single rod, an infinite number of equally spaced slits/rods (*i.e.*, a grating) forms a self-complementary system. The double slits studied here exhibit features of both extremes because the bridge separating the two slits may also be viewed as a rod, introducing an element of

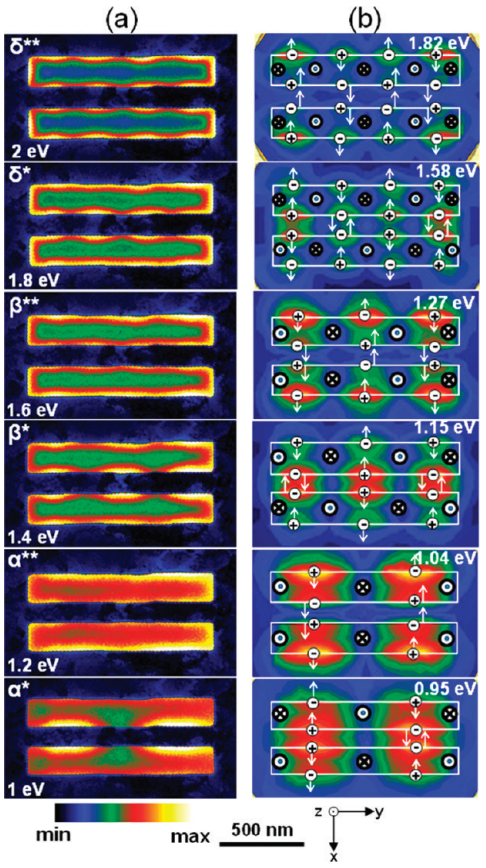

Figure 3. (a) Experimental EFTEM images acquired at energy losses of 1, 1.2, 1.4, 1.6, 1.8, and 2 eV and (b) calculated electric field strength |E|, vectors (black arrows), charge distributions and magnetic field vectors (pointing into and out of the page assigned by ⊗ and ⊙, respectively) at resonance energies (wavelengths) 0.95 eV (1.29 μm), 1.04 eV (1.19 μm), 1.15 eV (1.08 μm), 1.27 eV (0.98 μm), 1.58 eV (0.79 μm), and 1.82 eV (0.68 μm) for the double slit. The scale bar in (a) is also valid for (b).

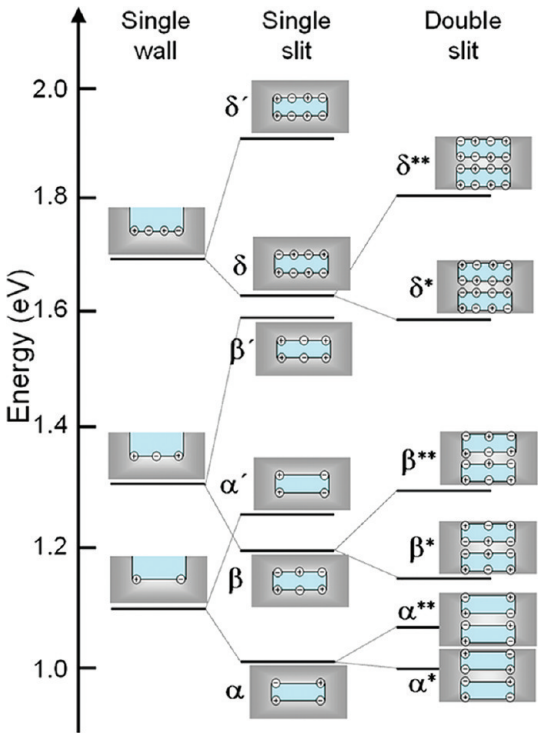

Figure 4. Energy-level diagram of the plasmon resonance modes found in the finite-element simulations for the single and double slits.

self-complementarity. It should as well be noted that Babinet's principle is strictly correct only for infinitely thin films that are perfectly conducting and flat. In real-life situations, the validity of Babinet's principle is approximate.[31] For slits in metal screens, this leads to the possibility of propagating SPs on the film surface, which may couple to and modify the spectral behavior of the LSPRs at the holes. Geometrically, the LSPRs experience effective width and length increases. For slits, this is due to the penetration of the fields into the surrounding metal, in rods due to the complementary penetration into the surrounding dielectric.[32,33]

The low-energy mode α^* has the same charges across the bridge (and opposite charges across the slits), whereas the high-energy mode α^{**} has opposite charges across both the bridge and the slits. If we consider the bridge as a rod-like structure, this is easily understood from Figure 1a. The energetic sequence of the α^* and α^{**} modes can also be shown by looking at the magnetic moments that are schematically shown for the six double slit modes in Figure 3. For the low-energy modes, there are six magnetic moments, and for the high-energy modes, there are 10 magnetic moments. Evidently, in the case of the modes α^*, β^*, and δ^*, the next-nearest magnetic moments have opposite sign and are therefore attractive. For modes α^{**}, β^{**}, and δ^{**}, the magnetic moments on both sides of the bridge are parallel, that is, repulsive. Thus, the double nanoslit system is in perfect Babinet complementarity to the conventional hybridization of direct (double nanorod) plasmonic structures.[28]

Figure 4 exquisitely recapitulates the electromagnetic coupling relations for our structures. HFSS simulations (not shown) validate the existence of two, three, and four E-field maxima at 1.1 eV (1.13 μm), 1.32 eV (0.94 μm), and 1.71 eV (0.73 μm), respectively, on the 1107 nm long single silver surface. The charge distributions and the energies observed for the expected lower and high-energy modes for single and double slits are all in agreement with Babinet's principle and plasmon hybridization theory, except the situation that the expected high-energy modes of double slits with charge distributions $++++$ and $++--$, designated as mode v and vi in Figure 1b, have been observed in neither the experiments nor the simulations.

CONCLUSIONS

EFTEM imaging allows hyperspectral imaging of eigenmodes in plasmonic nanostructures with exquisite spatial resolution in the nanometer range and short acquisition times. Here we apply EFTEM imaging

to SP eigenmodes in single and coupled nanoslits in a thin Ag film. We find close correspondence of experimental data with FEM simulations. We interpret the plasmonic modes as Fabry-Pérot-like SP interferences along the length of the slits. The transverse interactions are interpreted by considerations of Babinet complementarity. We find evidence for magnetic coupling between closely spaced slits ordering the energetic sequence of hybridized modes and note that the very same conclusions also follow from complementary considerations of electric coupling across the rod-like bridge separating the slits. The present results suggest new opportunities to tune resonances and electromagnetic coupling by considering not only the geometry of direct metallic nanostructures but also their Babinet complements.

MATERIALS AND METHODS

Specimen Preparation. A 100 nm thick silver film was deposited on a NaCl crystal (optically polished, Korth Kristalle GmbH, Kiel, Germany, Art. No. 10 40 106) by physical vapor deposition at 200 °C. Subsequently, the silver film was removed from the NaCl crystal by dissolving the substrate in distilled water and then transferring the film to a standard TEM 300 mesh Cu grid. On the grid, the Ag film is free-standing, which is advantageous for the interpretation of the measurements since effects due to the presence of a substrate do not occur. A rectangular single slit (210 nm × 1107 nm) and double slits (180 nm × 1070 nm) with 130 nm slit separation were drilled into the film by a focused ion beam (FIB) (FEI Nova Nano Lab). The thickness of the Ag film has been measured by a log-ratio method based on the comparison of the areas under the zero-loss peak, and the whole total area in an acquired EELS spectrum.[34]

Experimental Method. The experiments were carried out at the sub-electronvolt sub-angstrom microscope (SESAM) (Zeiss, Oberkochen, Germany) operated at 200 kV.[35,36] The SESAM is equipped with a field-emission gun, a symmetric electrostatic Omega-type electron monochromator,[37] and an in-column MANDOLINE filter.[38] The advantages of this combination of electron optical components are a high dispersion of the energy filter of about 6 μm/eV, an energy resolution better than 100 meV, and small non-isochromaticity of only 0.1 meV/nm.[36] The very high dispersion is important to obtain images from very narrow energy-loss ranges; an energy resolution better than 0.2 eV is mandatory especially for the infrared range of the spectrum because of the overlap of spectral features with the elastic zero-loss peak, and the excellent isochromaticity guarantees simple image interpretation over large fields of view. The perforated Ag thin films were investigated with the energy-filtering transmission electron microscopy (EFTEM) imaging technique. Both the monochromator slit and the energy-selecting slit in the energy filter had a width of 0.2 eV. A series of energy-filtered images were recorded in the energy-loss range from 0.4 to 5.0 eV using a step size of 0.2 eV. The images were recorded on a 2k × 2k CCD camera (Ultrascan, Gatan, USA) applying a binning of 4. Because of the variation of electron intensity in different energy-loss ranges, the acquisition time was automatically adjusted for each image. However, the acquisition time was not allowed to exceed 30 s in order to make specimen drift artifacts negligible. In order to eliminate camera artifacts due to scintillator afterglow, we started the image series at an energy loss of 5 eV, where the image intensity is lowest and recorded new dark-reference images after each energy-filtered image. All of the data have been processed using Gatan Digital Micrograph. The specimen drift in the image series was corrected by using a script described elsewhere.[39]

Eigenmode Simulations. In order to calculate the plasmonic eigenmodes of the rectangular slits in the Ag film, we used commercially available software (high-frequency structure simulator, HFSS 12, Ansoft, Inc., USA). This is based on the finite-element method (FEM) to solve Maxwell's equations using an adaptive mesh refinement with tetrahedral mesh units.[40–42]

Rectangular single and double slits (with the same dimensions as in the experiment) in a 100 nm thick silver film (2 μm × 2 μm) were simulated with this method. For the double slit, the distance between the two rectangles was 130 nm. The HFSS eigenmode solver was used to perform the calculations, where a spherical impedance boundary confined the volume around the rectangular hole. The radius of the sphere was chosen large enough not to affect the results of the simulation. We used the optical constants for silver reported in the literature.[43] The (real valued) relative electric permittivity and conductivity were then obtained, respectively, from the relations $\varepsilon_r = n^2 - k^2$ and $\sigma = \omega\varepsilon_0 2nk$, where ω is the angular frequency, n the index of refraction, and k the absorption constant.

Acknowledgment. We thank J. Dorfmüller for helpful discussions, U. Eigenthaler and I. Lakemeyer for specimen preparation, M. Laudien for the support with HFSS simulations. This research has been supported by the European Union under the Framework 6 program under a contract for an Integrated Infrastructure Initiative, Reference 026019 (ESTEEM).

REFERENCES AND NOTES

1. Gramotnev, D. K.; Bozhevolnyi, S.I. N. Plasmonics beyond the Diffraction Limit. *Nat. Photonics* **2010**, *4*, 83–91.
2. Luther, J. M.; Jain, P. K.; Ewers, T.; Alivisatos, A. P. Localized Surface Plasmon Resonances Arising from Free Carriers in Doped Quantum Dots. *Nat. Mater.* **2011**, *10*, 361–366.
3. El-Sayed, I. H.; Huang, X.; El-Sayed, M. A. Surface Plasmon Resonance Scattering and Absorption of Anti-EGFR Antibody Conjugated Gold Nanoparticles in Cancer Diagnostics: Applications in Oral Cancer. *Nano Lett.* **2005**, *5*, 829–834.
4. Lal, S.; Clare, S. E.; Halas, N. J. Nanoshell-Enabled Photothermal Cancer Therapy: Impending Clinical Impact. *Acc. Chem. Res.* **2008**, *41*, 1842–1851.
5. Kneipp, K.; Wang, Y.; Kneipp, H.; Perelmann, L. T.; Itzkani, I.; Dasari, R. R.; Feld, M. Single Molecule Detection Using Surface-Enhanced Raman Scattering. *Phys. Rev. Lett.* **1997**, *78*, 1667–1670.
6. Brongersma, M. L.; Zia, R.; Schuller, J. A. Plasmonics—The Missing Link between Nanoelectronics and Microphotonics. *Appl. Phys. A: Mater. Sci. Process.* **2007**, *89*, 221–223.
7. Zia, R.; Schuller, J. A.; Chandran, A.; Brongersma, M. L. Plasmonics—-The Wave of Chip Scale Device Technologies. *Mater. Today* **2006**, *9*, 20–27.
8. Pines, D.; Bohm, D. A Collective Description of Electron Interactions: II. Collective *vs* Individual Particle Aspects of the Interactions. *Phys. Rev.* **1952**, *85*, 338–353.
9. Ritchie, R. H. Plasma Losses by Fast Electrons in Thin Films. *Phys. Rev.* **1957**, *106*, 874–881.
10. Raether, H. *Surface Plasmons on Smooth and Rough Surfaces and on Gratings*; Springer-Verlag: Berlin, Heidelberg, 1988; pp 4−37.
11. Ebbesen, T. W.; Lezec, H. J.; Ghaemi, H. F.; Thio, T.; Wolff, P. A. Extraordinary Optical Transmission through Sub-wavelength Hole Arrays. *Nature* **1998**, *391*, 667–669.
12. Batson, P. E. Surface Plasmon Coupling in Clusters of Small Spheres. *Phys. Rev. Lett.* **1982**, *49*, 936–940.
13. Vogelgesang, R.; Dmitriev, A. Real-Space Imaging of Nanoplasmonic Resonances. *Analyst* **2010**, *135*, 1175–1181.
14. Nelayah, J.; Kociak, M.; Stephan, O.; Garcia de Abajo, F. J.; Tence, M.; Henrard, L.; Taverna, D.; Pastoriza-Santos, I.;

Liz-Marzan, L. M.; Colliex, C. Mapping Surface Plasmons on a Single Metallic Nanoparticle. *Nat. Phys.* **2007**, *3*, 348–353.
15. Nelayah, J.; Gu, L.; Sigle, W.; Koch, C. T.; Pastoriza-Santos, L.; Liz-Marzan, L. M.; van Aken, P. A. *Proceedings of the 14th European Microscopy Congress 2*; Springer: Berlin, 2008; p 243.
16. Nelayah, J.; Gu, L.; Sigle, W.; Koch, C. T.; Pastoriza-Santos, L.; Liz-Marzan, L. M.; van Aken, P. A. Direct Imaging of Surface Plasmon Resonances on Single Triangular Silver Nanoprisms at Optical Wavelength Using Low-Loss EFTEM Imaging. *Opt. Lett.* **2009**, *34*, 1003–1005.
17. Gu, L.; Sigle, W.; Koch, C. T.; Ögüt, B.; van Aken, P. A.; Talebi, N.; Vogelgesang, R.; Mu, J.; Wen, X.; Mao, J. Resonant Wedge Plasmon Modes in Single-Crystalline Gold Nanoplatelets. *Phys. Rev. B* **2011**, *83*, 195433/1–195433/7.
18. Schaffer, B.; Hohenester, U.; Trügler, A.; Hofer, F. High-Resolution Surface Plasmon Imaging of Gold Nanoparticles by Energy-Filtered Transmission Electron Microscopy. *Phys. Rev. B* **2009**, *79*, 041401/1–041401/4.
19. Sigle, W.; Nelayah, J.; Koch, C. T.; van Aken, P. A. Electron Energy Losses in Ag Nanoholes—From Localized Surface Plasmon Resonances to Rings of Fire. *Opt. Lett.* **2009**, *34*, 2150–2152.
20. Sigle, W.; Nelayah, J.; Koch, C. T.; Ögüt, B.; Gu, L.; van Aken, P. A. EFTEM Study of Surface Plasmon Resonances in Silver Nanoholes. *Ultramicroscopy* **2010**, *110*, 1094–1100.
21. Liu, N.; Giessen, H. Coupling Effects in Optical Metamaterials. *Angew. Chem., Int. Ed.* **2010**, *49*, 9838–9852.
22. Apell, S. P.; Echenique, P. M.; Ritchie, R. H. Sum Rules for Surface Plasmon Frequencies. *Ultramicroscopy* **1996**, *65*, 53–60.
23. Manjavacas, A.; Garcia de Abajo, F. J. Robust Plasmon Waveguides in Strongly Interacting Nanowire Arrays. *Nano Lett.* **2009**, *9*, 1285–1289.
24. Funston, A. M.; Novo, C.; Davis, T. J.; Mulvaney, P. Plasmon Coupling of Gold Nanorods at Short Distances and in Different Geometries. *Nano Lett.* **2009**, *9*, 1651–1658.
25. Merlin, R. Metamaterials and the Landau−Lifshitz Permeability Argument: Large Permittivity Begets High-Frequency Magnetism. *Proc. Natl. Acad. Sci. U.S.A.* **2009**, *106*, 1693–1698.
26. Falcone, F.; Lopetegi, T.; Laso, M. A. G.; Baena, J. D.; Bonache, J.; Beruete, M.; Marqués, R.; Martin, F.; Sorolla, M. Babinet Principle Applied to the Design of Metasurfaces and Metamaterials. *Phys. Rev. Lett.* **2004**, *93*, 197401/1–197401/4.
27. Zentgraf, T.; Meyrath, T. P.; Seidel, A.; Kaiser, S.; Giessen, H. Babinet's Principle for Optical Frequency Metamaterials and Nanoantennas. *Phys. Rev. B* **2007**, *76*, 033407/1–033407/4.
28. Halas, N. J.; Lal, S.; Chang, W. S.; Link, S.; Nordlander, P. Plasmons in Strongly Coupled Metallic Nanostructures. *Chem. Rev.* **2011**, *111*, 3913–3961.
29. Prodan, E.; Nordlander, P. Plasmon Hybridization in Spherical Nanoparticles. *J. Chem. Phys.* **2004**, *120*, 5444–5454.
30. Seo, M. A.; Koo, H. R. S. M.; Park, D. J.; Kang, J. H.; Suwal, O. K.; Choi, S. S.; Planken, P. C. M.; Park, G. S.; Park, N. K.; Park, Q. H. Terahertz Field Enhancement by a Metallic Nanoslit Operating beyond the Skindepth Limit. *Nat. Photonics* **2009**, *3*, 152–156.
31. Jackson, J. D. *Classical Electrodynamics*; John Wiley & Sons: New Jersey, 1999; pp 488−490.
32. Dorfmüller, J.; Vogelgesang, R.; Weitz, R. T.; Rockstuhl, C.; Etrich, C.; Pertsch, P.; Lederer, F.; Kern, K. Fabry-Pérot Resonances in One-Dimensional Plasmonic Nanostructures. *Nano Lett.* **2009**, *9*, 2372–2377.
33. Dorfmüller, J.; Vogelgesang, R.; Khunsin, W.; Rockstuhl, C.; Etrich, C.; Kern, K. Plasmonic Nanowire Antennas: Experiment, Simulation, and Theory. *Nano Lett.* **2010**, *10*, 3596–3603.
34. Egerton, R. F. *Electron Energy-Loss Spectroscopy in the Electron Microscope*; Plenum Press: New York, 1996; pp 302−307.
35. Koch, C. T.; Sigle, W.; Höschen, R.; Rühle, M.; Essers, E.; Benner, G.; Matijevic, M. SESAM: Exploring the Frontiers of Electron Microscopy. *Microsc. Microanal.* **2006**, *12*, 506–514.
36. Essers, E.; Benner, G.; Mandler, T.; Meyer, S.; Mittmann, D.; Schnell, M.; Höschen, R. Energy Resolution of an Omega-Type Monochromator and Imaging Properties of the MANDOLINE Filter. *Ultramicroscopy* **2010**, *110*, 971–980.
37. Kahl, F.; Rose, H. *Proceedings of the 11th European Conference on Electron Microscopy 1* Dublin, 1996; p 478.
38. Uhlemann, S.; Rose, S. MANDOLINE Filter—A New High Performance Imaging Filter for Sub-eV EFTEM. *Optik* **1994**, *96*, 163–178.
39. Schaffer, B.; Grogger, W.; Kothleitner, G. Automated Spatial Drift Correction for EFTEM Image Series. *Ultramicroscopy* **2004**, *102*, 27–36.
40. Parsons, J.; Hendry, E.; Sambles, J. R.; Barnes, W. L. Localized Surface-Plasmon Resonances and Negative Refractive Index in Nanostructured Electromagnetic Metamaterials. *Phys. Rev. B* **2009**, *80*, 245117/1–245117/6.
41. Degiron, A.; Smith, D. R. Numerical Simulations of Long-Range Plasmons. *Opt. Express* **2006**, *14*, 1611–1625.
42. Nemat-Nasser, S. C.; Amirkhizi, A. V.; Padilla, W. J.; Basov, D. N.; Nemat-Nasser, S.; Bruzewicz, D.; Whitesides, G. Terahertz Plasmonic Composites. *Phys. Rev. E* **2007**, *75*, 036614/1–036614/7.
43. Johnson, P. B.; Christy, R. W. Optical Constants of the Noble Metals. *Phys. Rev. B* **1972**, *6*, 4370–4379.